doi: 10.15407/ujpe62.09.0806

V.B. NEIMASH,[1] V. MELNYK,[1] L.L. FEDORENKO,[2] P.YE. SHEPELYAVYI,[2] V.V. STRILCHUK,[2] A.S. NIKOLENKO,[2] M.V. ISAIEV,[3] A.G. KUZMYCH[3]

[1] Institute of Physics, Nat. Acad. of Sci. of Ukraine
(46, Nauky Ave., Kyiv 03028, Ukraine; e-mail: neimash@gmail.com)
[2] V.E. Lashkaryov Institute of Semiconductor Physics, Nat. Acad. of Sci. of Ukraine
(e-mail: neimash@gmail.com)
[3] Taras Shevchenko National University of Kyiv, Faculty of Physics
(64/13, Volodymyrs'ka Str., Kyiv 01601, Ukraine)

PACS 61.72.uf, 61.72.uj, 73.40.Vz, 78.30.Fs, 81.07.Bc

TIN-INDUCED CRYSTALLIZATION OF AMORPHOUS SILICON UNDER PULSED LASER IRRADIATION

Tin-induced crystallization of amorphous silicon in thin-film Si–Sn–Si structures under the influence of laser irradiation of various types has been studied, by using Raman scattering. The size and concentration dependences of Si nanocrystals on the power of 10-ns and 150-μs laser pulses with a wavelength of 535 or 1070 nm are experimentally measured and analyzed. A possibility of effective tin-induced transformation of silicon in a-Si layers 200 nm in thickness from the amorphous to crystalline phase within 10 ns time interval under the action of laser light pulses is demonstrated. The theoretical calculation of the spatial temperature distribution and its time evolution in the area of the laser beam action is used to interpret the experimental results.

Keywords: solar cells, thin films, nanocrystals, silicon, tin, metal-induced crystallization.

1. Introduction

The film composite of Si nanocrystals in an amorphous Si matrix (nc-Si), owing to some of its physical properties that are advantageous for devices of photo-electric conversion of solar energy – in particular, these are the quasidirect band-gap mechanism of light absorption, the dependence of the energy gap width on the size of nanocrystals, resistance to the Staebler–Wronski effect, and possibility of its formation on flexible substrates – is considered to be a promising material for the next generation of solar cells based on quantum dots [1]. The application of nanocomposite silicon as a basic material allows the efficiency of solar cells to be substantially raised by creating polymorphic heterostructures of the cascade type [2, 3] and reducing the costs of solar cell manufacture due to the advantages of thin-film and roll technologies [4, 5].

The main difficulties that hinder the implication of nc-Si advantages into practice include an insufficient development of technologies aimed at controlling the size and the concentration of Si nanocrystals provided economically reasonable rates of film fabrication. Therefore, despite that there are a considerable number of already available technologies for the nc-Si manufacture, a lot of attention is paid to their improvement and to the search for new ones (see, e.g., works [6–12]).

One of the promising ways in this direction is the application of the phenomenon of metal-induced crystallization (MIC) of amorphous silicon (a-Si) [13–17]. In particular, a possibility to form Si nanocrystals 2–7 nm in dimensions and with a phase volume fraction of up to 80% in the a-Si matrix with the help of the low-temperature tin-induced Si crystallization was demonstrated in [18–20]. Those experimental results were interpreted with the use of a new mechanism of MIC, which was proposed in works [20–22] and considerably differs from those known for other metals [13, 15–17]. According to this mechanism, silicon nanocrystals are formed as a result of the cyclic repetition of their formation and decay pro-

cesses in the supersaturated solution of silicon in tin that emerges in a narrow eutectic layer at the a-Si/Sn interfaces between tin microdroplets and the bulk of amorphous Si.

In work [23], it was shown that the process of tin-induced crystallization of amorphous silicon can be stimulated by laser irradiation. This fact allows the Raman scattering to be used in order to measure the temperature, size of nanocrystals, and volume occupied by them in the course of their formation. Simultaneously, the crystallization can be controlled by changing the laser radiation intensity and the duration of its application.

The aim of this work is to determine the temperature and temporal parameters of MIC in the a-Si/Sn system and to estimate the role of photoionization in the processes of Si nanocrystal formation, as well as the prospects of the laser radiation application to control the size and the concentration of Si nanocrystals at the tin-induced crystallization of amorphous silicon. We studied how the pulsed laser radiation intensity I affects the size of nanocrystallites and the volume fraction occupied by them in the films of an nc-Si/a-Si composite. For this purpose, we used pulsed laser radiation with the power in the interval 1.4×10^4–2.18×10^8 W/cm^2, pulse durations $\tau = 10$ ns and 150 μs, and light wavelengths $\lambda = 535$ mn and 1.07 μm.

2. Experimental Part

The cross-sections of examined three-layer film structures are schematically shown in Fig. 1. The structures were fabricated by consecutively depositing silicon and tin onto a single-crystalline silicon (c-Si) substrate at a temperature of 150 °C by the method of thermal evaporation in vacuum. All three deposition stages were performed in the same vacuum chamber, without loss of vacuum, at a residual pressure of 10^{-3} Pa, and consecutively using three different evaporators. Si (99.999%) and Sn (99.92%) were sputtered. The substrate thickness was $d = 1$ mm. The thicknesses of layers X (adjacent to the substrate), Y, and Z are quoted in Table together with the parameters of laser irradiation.

The specimen surface was divided into 0.5×0.5 cm^2 rectangular sections. Each of the latter was irradiated with single laser pulses in the programmed scanning mode. The degree of laser spot overlapping could be

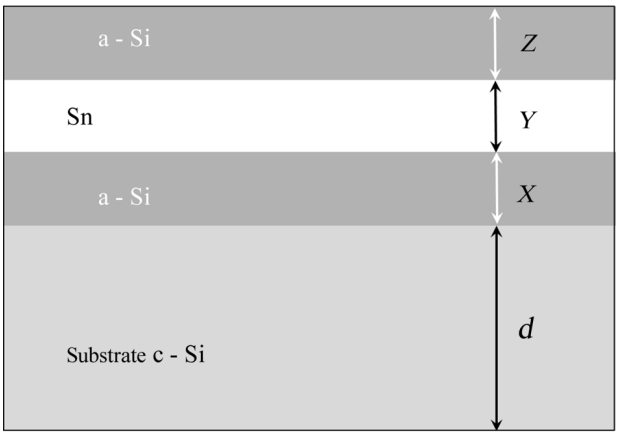

Fig. 1. Schematic diagram of the cross-section of researched a-Si/Sn/a-Si/c-Si layered structures. The substrate thickness $d = 1$ mm

controlled at a certain power in one of the irradiation modes quoted in Table. In our experiment, the light beam diameter amounted to 70 μm, and the scanning step to 50 μm. Therefore, we may assume that the whole area of each section was subjected to the identical irradiation.

Different sections were irradiated, by using pulses with different powers. The laser light power was controlled by means of a focusing system, the attenuation by a stack of glass plates, and by using neutral gray filters. In such a manner, a number of sections were obtained on each specimen. Each of the sections was irradiated by light with a different power, but with the same pulse duration and light wave-

Specimens and regimes of their laser treatment

Specimen No.	Layer thicknesses $X:Y:Z$, nm	Laser wavelength, nm	Pulse duration	Light power interval, W · cm^{-2}
1	50 : 100 : 200	1070	150 μs	$(1{,}4–2{,}9)\times10^4$
2	50 : 100 : 200	1070	150 μs	$1{,}3\times10^5$
			10 ns	$(5{,}3–18{,}0)\times10^7$
3	50 : 100 : 200	1070	150 μs	$(2{,}9–7{,}8)\times10^4$
4	50 : 100 : 200	535	10 ns	$(5{,}5–8{,}5)\times10^6$
5	50 : 100 : 200	535	10 ns	$(8{,}5–21{,}8)\times10^6$
6	50 : 100 : 200	1070	150 μs	$(2{,}3–6{,}9)\times10^4$
6 : 1	50 : 100 : 200	1070	10 ns	$(7{,}4–15{,}3)\times10^7$
6 : 2	50 : 100 : 200	535	10 ns	$(3{,}5–10{,}3)\times10^6$
7	0 : 100 : 200	1070	10 ns	$(8{,}4–52{,}0)\times10^7$
8	0 : 100 : 200	1070	10 ns	$(2{,}0–21{,}8)\times10^7$

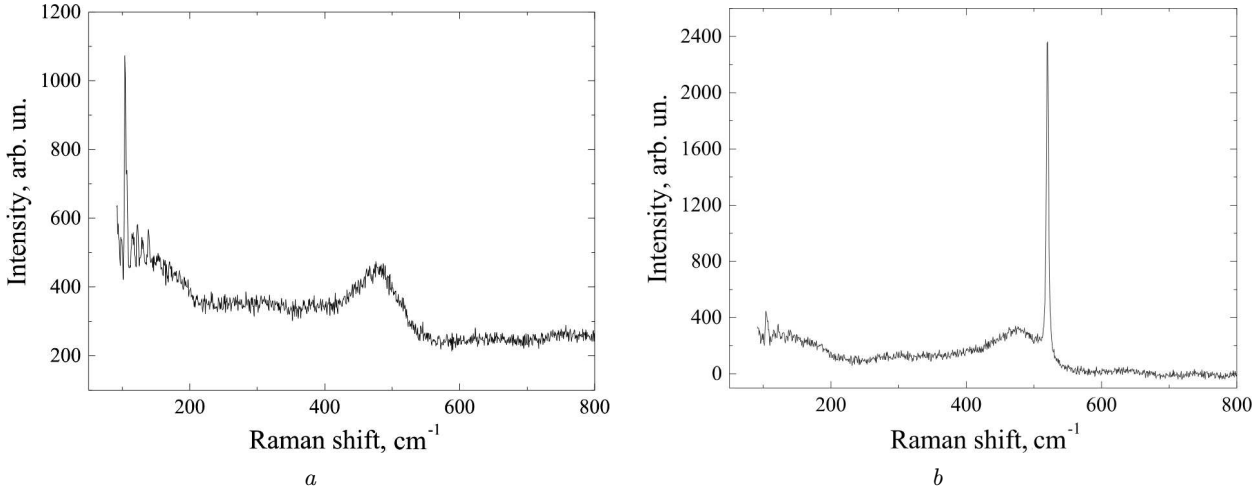

Fig. 2. Typical Raman spectra for amorphous (*a*) and partially crystallized (*b*) silicon

length. The phase composition of each section was afterward researched by measuring and analyzing the Raman spectrum of the section. In addition, the surface area around the Raman spectrum measurement place was photographed in an optical microscope.

Micro-Raman spectra were measured at room temperature in the back-scattering geometry on a Horiba Jobin Yvon T64000 spectrometer equipped with a confocal microscope Olympus BX41 and a thermoelectrically cooled CCD detector. The spectral resolution amounted to 0.15 cm^{-1}. The Raman spectra were excited, by using the Ar^+–Kr^+ laser line with the wavelength $\lambda_{ex} = 488$ nm. The exciting radiation was focused onto a spot with an area of about 5 μm^2 on the researched specimen surface with the use of an objective Olympus 10×0.25.

The measurements were carried out at an exciting laser irradiation power of 1 mW, which provided a power density of about 20 kW/cm^2 at the specimen surface. This power did not result in a substantial laser-induced heating of the specimens in comparison with room temperature.

3. Results and Their Discussion

The typical Raman spectra of initial specimens in an interval of 100–850 cm^{-1} are exhibited in Fig. 2. Before the laser treatment (panel *a*), the spectra of specimens 7 and 8 (see Table) contained only a wide band with a maximum at 475 cm^{-1}, which is characteristic of amorphous Si [24]. After the laser treatment of the specimens in certain regimes, there appeared an addition narrow band in their spectra with a maximum in an interval from 500 to 520 cm^{-2} (panel *b*), which corresponds to the nanocrystalline phase of silicon [24, 25]. This is a result of MIC of amorphous silicon under the influence of laser irradiation [23]. The initial spectra of three-layer specimens 1 to 6 : 2 (see Table) demonstrated the both bands. In other words, those specimens contained both the amorphous and crystalline phases even before their laser treatment. They were used to study the possibilities of the laser irradiation action on nanocrystals that were formed beforehand.

The size L of nanocrystals and the volume fraction X_C occupied by them in the examined specimens were determined, by carrying out the computer-assisted approximation of Raman spectra in the framework of the theory of spatially confined phonons [24, 25] with simplifications described in work [20]. In particular, it was found that the initial parameters of crystallinity in specimens 1, 2, 3, 6, and 6 : 1 were as follows: $L = 1.5$ nm and $X_C = 48\%$. Below, the variation of the indicated parameters under the action of single laser pulses with various intensities, durations, and wavelengths is considered.

Influence of the intensity of laser irradiation with $\lambda = 1.07$ μm and $\tau = 150$ μs on the a-Si/Sn/a-Si layered structure. Figure 3 illustrates how the size of nanocrystals and the volume fraction occupied by them change with a growth of the laser irradiation intensity for specimens 3 and 6 after the scanning them with single pulses. One can see that, from an inten-

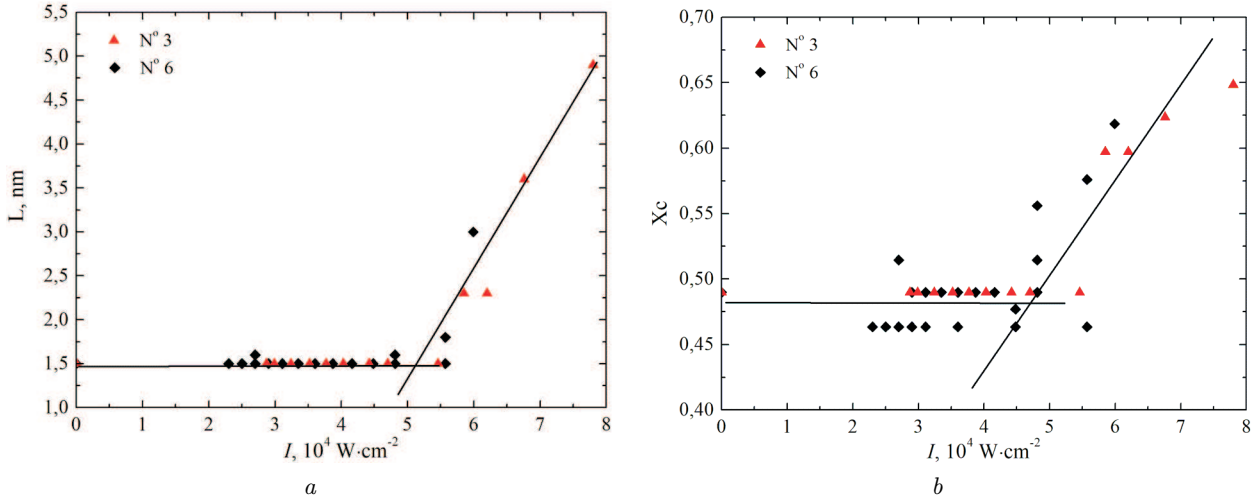

Fig. 3. Dependences of nanocrystal size (*a*) and nanocrystal volume fraction (*b*) on the laser irradiation power for specimens 3 and 6. Symbols correspond to experimental data, and lines to their linear fitting

sity of about 5.5×10^4 W/cm^2, the nanocrystal sizes and the fraction of the crystalline phase increase with the laser light power. In particular, the increase of irradiation power from 5.5×10^4 to 7.8×10^4 W/cm^2 resulted in a growth of the nanocrystal size from 1.5 to 5.0 nm. The variation of the crystalline phase fraction is changed in a qualitatively similar manner. A larger spread of X_C-values in comparison with the spread of nanocrystal sizes was caused by a higher statistical error, while calculating this parameter.

Those results confirm the conclusions of work [23] about the influence of the irradiation intensity on the size and the concentration of crystals at MIC in a-Si/Sn/a-Si structures subjected to a continuous laser irradiation. As one can see from Fig. 3, this influence has a threshold character, by starting from a power of $5{\times}10^4$ W/cm^2, which can be associated, in particular, with reaching the melting temperature in the tin layer of researched structures. According to work [22], the transition of tin into the liquid state is a required condition for MIC to take place in amorphous Si.

Attention should be paid to that, as I increases from 5.5×10^4 to 8×10^4 W/cm^2 (and, accordingly, the temperature in the region of laser beam action grows), the volume fraction of the crystalline phase grows much more slowly than the growth of nanocrystal sizes, although the crystal volume equals L^3. This fact means that only an insignificant number of initial nanocrystals serve as nuclei for the precipitation of Si from its solution in Sn. The main part of them do not grow or even are dissolved, since their size is less than the size of a critical nucleus.

Figure 4 demonstrates the typical images obtained with the help of an optical microscope for the surface sections of specimens, both initial and irradiated in the subthreshold power interval (Fig. 4, *a*), as well as for a section irradiated with pulses of maximum power (Fig. 4, *b*). Since a laser beam about 2 mm in diameter was used to excite Raman spectra, the analysis of the spectra measured from various parts of specimens showed that dark spots correspond to regions with higher concentrations of nanocrystals in the amorphous matrix in comparison with the corresponding parameter in the light background. One can see that such regions were already observed for initial specimens. They remained invariable after the laser irradiation with subthreshold intensities. For intensities above the threshold value, the sizes of those regions increased. The growth of the total area of dark regions correlated with the growth of the volume fraction X_C occupied by nanocrystals, which was determined from the Raman spectra.

Influence of the laser irradiation intensity with $\lambda = 1.07$ μm *and* $\tau = 10$ ns *on the a-Si/Sn/a-Si layered structure.* Specimens 2 and 6 : 1 similar to the previous ones (the three-layer a-Si/Sn/a-Si structure 50 nm : 100 nm : 200 nm, partially crystallized: $L = 1.5$ nm, $X_C = 48\%$) were irradiated with light with the same wavelength $\lambda = 1070$ nm, but using pulses four orders of magnitude shorter (10 ns) and three or-

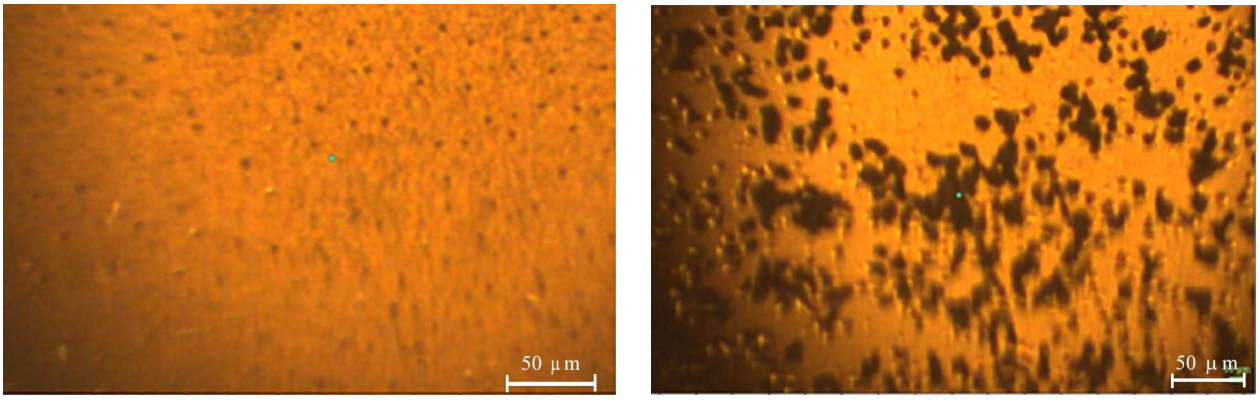

a *b*

Fig. 4. Optical microscope images of the specimen surface sections after laser irradiation with the intensity $I \leq 5 \times 10^4$ W/cm^2 (*a*) and $I = 8.2 \times 10^4$ W/cm^2

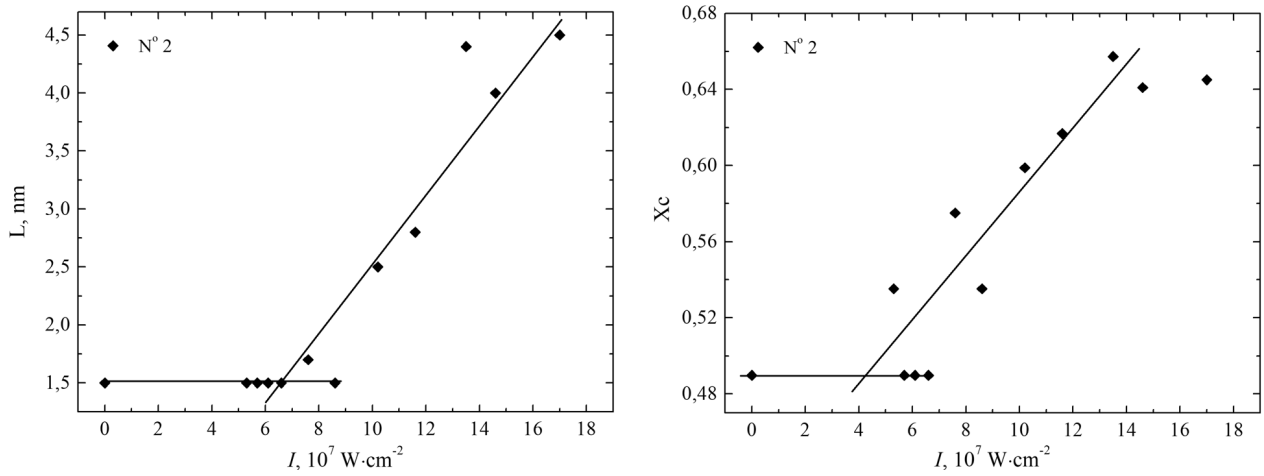

a *b*

Fig. 5. Dependences of the crystal size (*a*) and the volume fractions occupied by crystals (*b*) in the external layer of specimen 2 on the laser irradiation intensity. Symbols correspond to experimental data, and lines to their linear fitting

ders of magnitude more powerful (10^7 W/cm^2). The influevce of this irradiation on the parameters of silicon crystallinity are shown in Fig. 5. One can see that, as in the previous case, the threshold character of the crystallization dependence on the intensity of laser irradiation takes place (the intensity threshold $I = 7.5 \times 10^7$ W/cm^2). As in the previous case, the microscope images testify to the correlation between the intensity of laser pulses and the growth of the total area of dark crystallization spots, when the intensity exceeds some threshold.

Knowing the intensity and duration of laser pulses in both cases, it is easy to evaluate and to compare the absorbed energy densities at the crystallization threshold: $E^{\rm tc}{=}I\,\tau$. It turned out that the absorbed energy per unit area equals $E_1^{\rm tc} = 8.3$ J/cm^2 in the former and $E_1^{\rm tc} = 0.75$ J/cm^2 in the latter case. This means that, in the case of more powerful laser irradiation, the energy that is an order of magnitude lower is required to start MIC. This fact can be explained in at least two ways: by a stimulating influence of the photoionization [23, 26] or by a stronger heating action of nanosecond pulses in comparison with microsecond ones owing to the heatsink inertia [27, 28].

Figure 6 demonstrates the experimental dependences of the crystal size and the volume fraction of the crystalline phase on the power of 10-ns pulses obtained for specimen 7, which was purely amorphous in

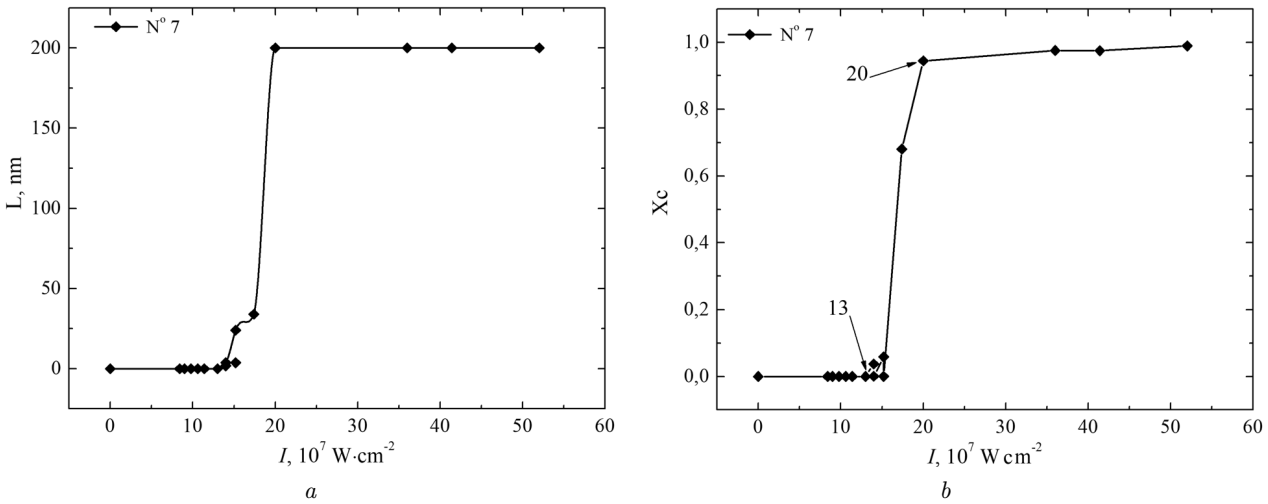

Fig. 6. Dependences of the size of Si nanocrystals (a) and the volume fraction occupied by them (b) on the 10-nc laser pulse power for specimen 7

the initial state. Pulses with a power lower than $I = 15 \times 10^7$ W/cm^2 did not stimulate phase transformations in the amorphous film. As the power increased, the film structure was modified: there appeared a crystalline component. The crystal size exceeded 10 nm at once. At the powers $I = 20 \times 10^7$ W/cm^2 and higher, the Raman spectra revealed only single-crystalline silicon in the substrate. Hence, in the power interval from 1.5×10^7 to 2.0×10^7 W/cm^2, the amorphous film collapsed without a substantial crystallization. A qualitatively similar behavior was observed for specimen 8, which also did not contain crystal nuclei.

Thus, unlike amorphous-crystalline specimens 2 and 6, which were considered above and in which the growth of the crystalline phase with I was clearly observed, MIC did not take place in amorphous specimens 7 and 8 without crystal nuclei subjected to a similar laser treatment. Therefore, we may assert that MIC includes the nucleus formation stage (the latent period), which lasts for more than 10 ns, and the stage of their quick multiple growth (from 1.5 to 4.5 nm) within a time interval of about 10 ns.

Influence of the laser irradiation intensity with $\lambda = 535$ nm and $\tau = 10$ ns on the a-Si/Sn/a-Si layered structure. Unlike light with the wavelength $\lambda = 1.07$ μm, which is weakly absorbed in a-Si and mainly heats up the tin layer in the researched structures, light with $\lambda = 535$ nm is almost completely absorbed in the external layer of amorphous silicon. Specimens 4, 5, and 6 : 2 were irradiated with laser light with the wavelength $\lambda = 535$ nm, the pulse duration $\tau = 10$ ns (as was in the previous case with $\lambda = 1.07$ μm), and in the power interval from $I = 10^6$ W/cm^2 to $I = 10^7$ W/cm^2.

The results of measurements of the Raman spectra and their analysis are shown in Fig. 7. One can see that the spread of the crystallinity parameter values is much larger than in the previous researches. This fact can be a consequence of the non-uniform phase transformation in the external a-Si film. Note that every point of the plot corresponds to different sections on the surface treated with pulses of a laser beam 70 μm in diameter and with a scanning step of 50 μm. At the same time, the diameter of the exciting laser beam at the Raman spectrum measurement amounted to about 2 μm. It is evident that, in the case of long-wave light ($\lambda = 1.07$ μm) that was mainly absorbed in the heat-conducting metal layer of examined structures, possible nonuniformities of heating in the laser-spot cross-section had enough time to be smoothed out during the laser pulse action, unlike the case of short-wave light ($\lambda = 535$ nm) absorbed in the weakly heat-conducting layer of amorphous silicon. Really, a typical size of the heated region in the material under the action of a pulse source can be estimated from the relation [29, 30]

$$l_{\text{th}} = [(D_{\text{th}} + D)\,\tau]^{1/2},$$

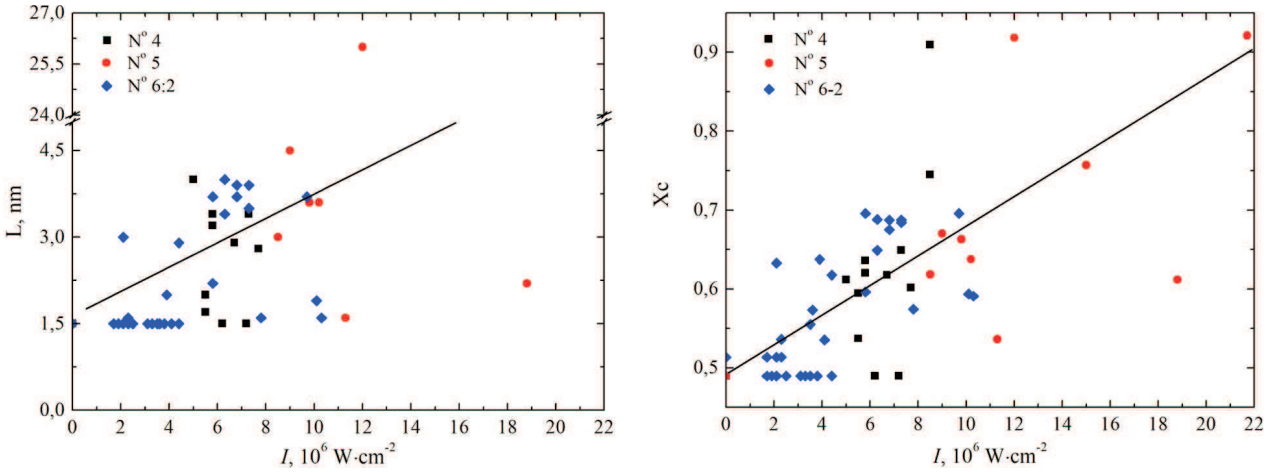

a *b*

Fig. 7. Dependences of the size of Si nanocrystals (*a*) and the volume fraction occupied by them (*b*) on the laser pulse power for specimens 4, 5, and 6 : 2

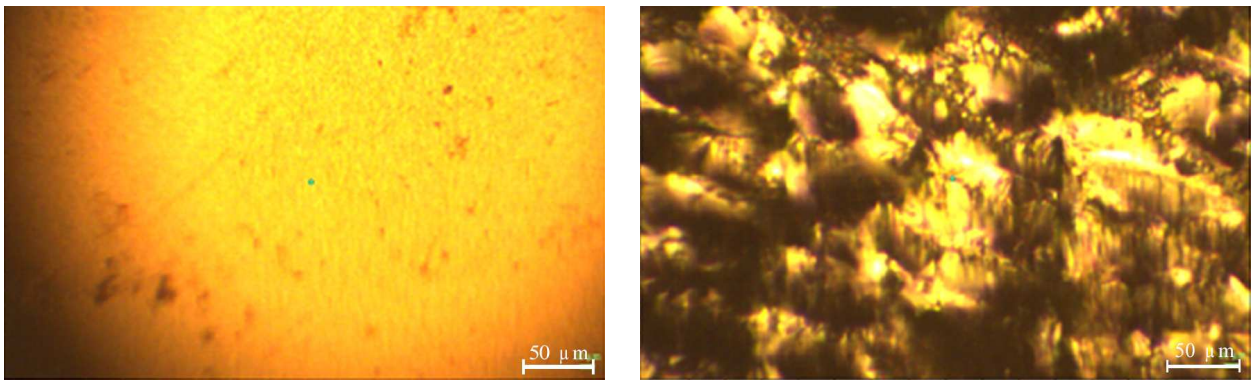

a *b*

Fig. 8. Influence of the laser pulse (535 nm, 10 ns) intensity on the surface of a-Si without nuclei (optical microscope images). $I = 0$ (*a*) and 8.2×10^4 W/cm^2 (*b*)

where D_{th} is the temperature conductivity, D the coefficient of bipolar diffusion of nonequilibrium charge carriers (for semiconductors), and τ the laser pulse duration. For tin, $D_{\text{th}} = 0.37$ cm^2/s [31], so that the characteristic size of the heated area within the time interval $\tau = 10 \times 10^{-9}$ s amounts to $l_{\text{th}} = 6.1 \times 10^{-5}$ cm.

At the same time, in amorphous silicon, the coefficient of green light absorption amounts to $\alpha = 6 \times 10^4$ cm^{-1}, the characteristic absorption depth to $l_\alpha = 1/\alpha = 1.6 \times 10^{-5}$ cm, and the thermal depth to $l_{\text{th}} = 8 \times 10^{-6}$ cm [34, 35]. In this case, the heating depth is determined by the largest quantities, i.e. by the absorption depth $1/\alpha$. However, in the lateral direction (along the surface), the thermal depth is actual. The corresponding size is by an order of magnitude smaller than the thickness of the external amorphous silicon layer in the researched structures. Owing to worse heatsink conditions, the maximum temperature of the local heating increases, as well as the temperature gradient. This can result in larger local deformation strains and, accordingly, in larger damages to the external a-Si layer, even despite that the power of 10-ns pulses is an order of magnitude lower at short-wave irradiation than at long-wave one. Really, from Fig. 8, where the micrographs of the surface of examined specimens before laser irradiation are depicted, one can see that this kind of laser treat-

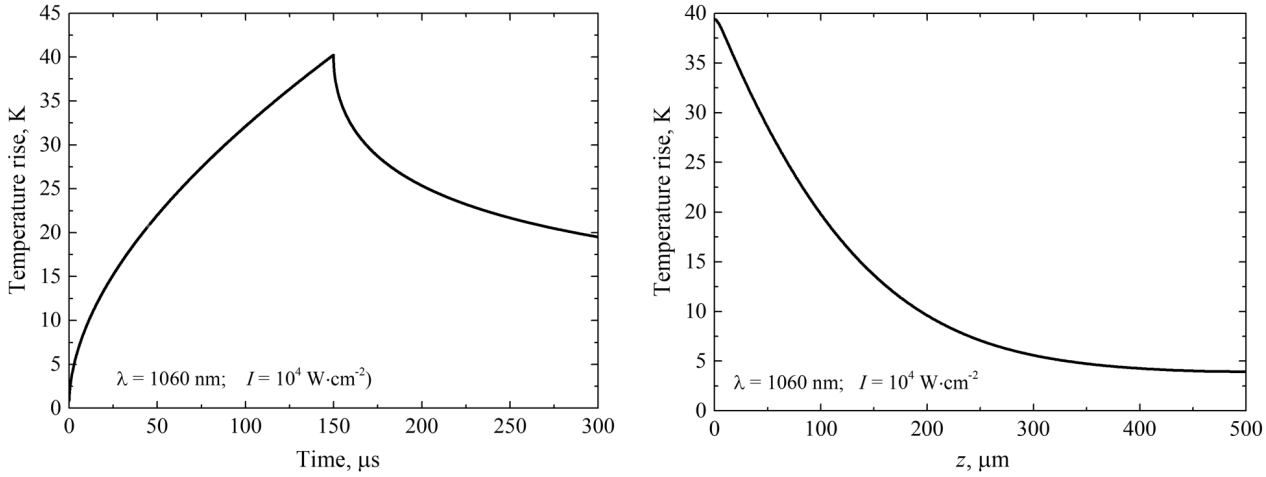

Fig. 9. Theoretical temperature rise at the surface of an irradiated specimen during the laser pulse action and immediately after it (a). Temperature rise distribution across the specimen thickness at the end of a laser pulse (b)

ment essentially changes the surface state in comparison with the initial one.

For the numerical calculation of the temperature conditions required for MIC to take place under a pulsed laser irradiation, let us consider the formation of a nonequilibrium temperature distribution in the one-dimensional approximation (across the thickness of researched structures). For this purpose, let us use the one-dimensional equation of heat conductivity, which is based on the Fourier law,

$$\rho c \frac{\partial \theta}{\partial t} = \left(\frac{\partial}{\partial z} \kappa \frac{\partial \theta}{\partial z} \right) + P(z,t),$$

where c is the specific heat capacity of the studied medium, ρ its density, κ the coefficient of heat conductivity, and $P(z,t)$ a function that characterizes the spatial and temporal distributions of heat sources in bulk. This approximation provides good temperature estimations in the region of the laser beam action, if its diameter considerably exceeds the thermal diffusion length [36, 37].

In the linear approximation, the spatial and temporal components of the distribution can be separated:

$$P(z,t) = f(z)\, g(t).$$

In the analyzed case, the spatial distribution of heat sources in bulk can be expressed in the form

$$f(z) = I_0 \alpha(z) \exp\left(\int_0^z \alpha(z')\, dz' \right),$$

where $\alpha(z)$ is the spatial distribution of the optical absorption coefficient. In all variants, the condition of temperature rise absence in the examined structure, $\theta(z,0) = 0$, was used as the initial one.

Let us analyze the laser-induced heating caused by a 150-μs pulse. In this case, the length of the laser pulse front is much shorter than its total duration. Therefore, the pulse form was taken to be rectangular:

$$g(t) = \begin{cases} 1, & t \le \tau, \\ 0, & t > \tau, \end{cases}$$

where $\tau = 150$ μs is the pulse duration. Since the latter parameter is much longer than the characteristic time of heat propagation in the sputtered layer, we considered an approximation of heat propagation in the crystalline substrate. The bulk heat sources in the modified layer were considered at that as a surface source:

$$\kappa \frac{\partial \theta}{\partial z}\bigg|_{z=0} = P_s(t), \quad P_s(t) = \int_0^{Z+Y+X} P(z,t)\, dz.$$

In addition, we used the boundary condition corresponding to the absence of a heat flow from the rear specimen surface,

$$\kappa \frac{\partial \theta}{\partial z}\bigg|_{z=Z+Y+X+d} = 0.$$

The resulting time dependence of the temperature at the specimen surface is depicted in Fig. 9, a for a

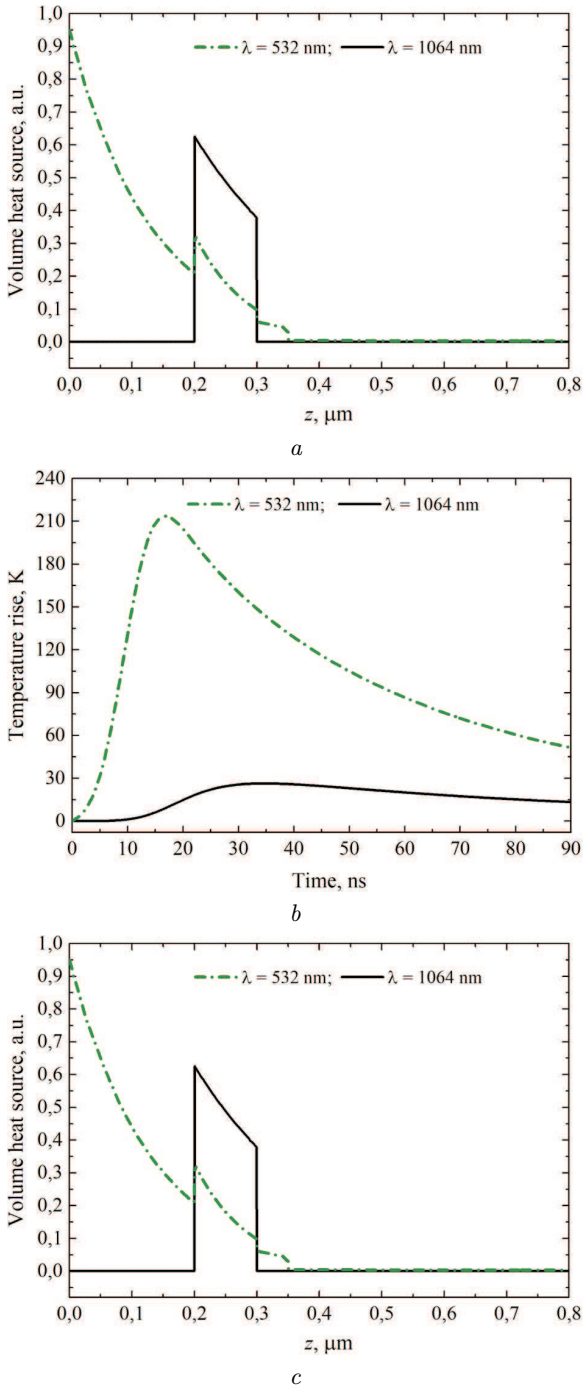

Fig. 10. Theoretical distribution of heat sources across the thickness of the Si–Sn–Si structure (a). Temperature evolution at the structure surface (b). Temperature fields at irradiation with 10-nanosecond pulses of infra-red (solid curve) and green (dash-dotted curve) lasers with a power of 1 MW/cm^2 at the time moment $t = 2\tau$ (c)

laser irradiation power of 10^4 W/cm^2. A typical spatial temperature distribution in the researched structure at a time moment $t = \tau$ is shown in Fig. 9, b.

According to Fig. 5, the structural state transformation threshold is reached in an intensity interval near 5×10^4 W/cm^2, i.e. when the intensity is five times higher than that used in the calculation, whose results are shown in Fig. 9. Therefore, in order to estimate the temperature at an intensity of 5×10^4 W/cm^2 in the linear approximation, we multiplied the temperature obtained for an intensity of 10^4 W/cm^2 by five and added the room temperature (300 K). The result corresponds to the maximum temperature at the surface:

$$300 \text{ K} + \frac{40 \text{ K}}{\text{W/cm}^2} \times 5 \text{ W/cm}^2 = 500 \text{ K}.$$

This temperature is close to the tin melting temperature (503 K). At a maximum power of about 8×10^4 W/cm^2 (see Fig. 4), the calculated temperature amounts to

$$300 \text{ K} + \frac{40 \text{ K}}{\text{W/cm}^2} \times 8 \text{ W/cm}^2 = 620 \text{ K},$$

i.e. about 350 °C, which agrees with the data of previous works concerning the temperature of the tin-induced crystallization of amorphous silicon [18–21].

In the case of nanosecond pulses, an essential role in the action of a laser pulse on the temperature is played by the spatial distribution of the thermal and optical parameters in the irradiated structure. Therefore, the indicated spatial distributions were considered in more details in this case. In particular, Fig. 10 demonstrates the spatial distributions of heat sources $f(z)$ and the temporal distributions of the temperature at the structure surface for two wavelengths (532 and 1064 nm) at a laser pulse power of 1 MW/cm^2.

As one can see from Fig. 10, a, in the case of infrared irradiation, the medium heating is mainly connected with the radiation absorption in the tin layer. In this case, the time distribution of the intensity in a laser pulse was regarded to be described by the Gaussian function

$$g(t) = \exp\left[-4 \ln 2 \frac{(t-\tau)^2}{\tau^2}\right].$$

As is seen from Fig. 10, b, the temperature at the structure surface at this power is close to the tin

melting temperature in the case of irradiation with the wavelength $\lambda = 532$ nm, which correlates with the data presented in Fig. 7, i.e. the crystallization begins already at the minimum intensity of a laser pulse. An intensity of 1 W/cm^2 is not enough to start the crystallization in the case of irradiation with light with the wavelength $\lambda = 1070$ nm. However, at an intensity of 60 MW/cm^2, when the crystallization threshold was observed experimentally, the temperature in the near-surface layer, according to calculations in the linear approximation, should reach

$$300 \text{ K} + \frac{30 \text{ K}}{\text{W/cm}^2} \times 60 \text{ W/cm}^2 = 2100 \text{ K}$$

and considerably exceeds the tin melting temperature. This discrepancy between experimental data and the results of model calculations can be a manifestation of the nonlinear optical phenomena, in particular, the absorption saturation effect [38]. We may assume that the electron density of states substantially decreases in the nanofragments in comparison with that in bulk. Therefore, the optical absorption and the corresponding heating could be considerably lower. Nanostructuring in thin tin layers in similar Si/Sn/Si structures was observed in work [20], in which the conditions of specimen fabrication were close to those used in this work.

4. Conclusions

The coincidence of the temperatures, at which the structure-phase changes begin and tin melts, confirms the scenario of the tin-induced crystallization of amorphous silicon as a process of cyclic formation and decay of a liquid silicon solution in tin, which was proposed in works [20,21]. The presence of two stages in MIC–the long-term latent period of nucleus formation and the short-term stage of nucleus growth–is typical of solution decay processes, which is also an argument in favor of the indicated mechanism. The results obtained testify to a possible influence of the photoionization on MIC of amorphous silicon.

In view of the high rate of amorphous silicon crystallization induced by tin (10^{-8}–10^{-4} s), its stimulation by pulsed light irradiation can form a basis for new technologies to control the size of nanocrystals, when manufacturing nc-Si films. In addition to the already mentioned task of constructing the cascade-type silicon photo-electric transducers, the results obtained also concern the creation of the so-called "all-Si" tandem solar cells, when silicon nanoclusters are formed between dielectric layers (such as SiO_2, Si_3N_4, and SiC [39,40]); the development of effective silicon-based gas sensors, in which the nanocluster catalysts of transition metals are used [41,42]; the manufacture of effective systems for the solid-state hydrogen storage on the basis of nanocomposite silicon structures [43,44]; and so forth.

1. M.C. Beard, J.M. Luther, A.J. Nozik. The promise and challenge of nanostructured solar cells. *Nature Nanotechn.* **9**, 951 (2014).
2. Z.I. Alferov, V.M. Andreev, V.D. Rumyantsev. Solar photovoltaics: Trends and prospects. *Semiconductors* **38**, 899 (2004).
3. B. Yan, G. Yue, X. Xu, J. Yang, S. Guha. High efficiency amorphous and nanocrystalline silicon solar cells. *Phys. Status Solidi B* **207**, 671 (2010).
4. N.S. Lewis. Toward cost-effective solar energy use. *Science* **315**, 798 (2007).
5. R. Søndergaard, M. Hösel, D. Angmo, T.T. Larsen-Olsen, F.C. Krebs. Roll-to-roll fabrication of polymer solar cells. *Mater. Today* **15**, 36 (2012).
6. M. Birkholz, B. Selle, E. Conrad, K. Lips, W. Fuhs. Evolution of structure in thin microcrystalline silicon films grown by electron-cyclotron resonance chemical vapor deposition. *J. Appl. Phys.* **88**, 4376 (2000).
7. B. Rech, T. Roschek, J. Müller, S. Wieder, H. Wagner. Amorphous and microcrystalline silicon solar cells prepared at high deposition rates using RF (13.56 MHz) plasma excitation frequencies. *Sol. Energy Mater. Sol. Cells* **66**, 267 (2001).
8. M.K. van Veen, C.H.M. van der Werf, R.E.I. Schropp. Tandem solar cells deposited using hot-wire chemical vapor deposition. *J. Non. Cryst. Solids* **338–340**, 655 (2004).
9. Y. Mai, S. Klein, R. Carius, H. Stiebig, L. Houben, X. Geng, F. Finger. Improvement of open circuit voltage in micro-crystalline silicon solar cells using hot wire buffer layers. *J. Non. Cryst. Solids* **352**, 1859 (2006).
10. H. Li, R.H. Franken, R.L. Stolk, C.H.M. van der Werf, J.K. Rath, R.E.I. Schropp. Controlling the quality of nanocrystalline silicon made by hot-wire chemical vapor deposition by using a reverse H_2 profiling technique. *J. Non. Cryst. Solids* **354**, 2087 (2008).
11. R. Amrani, F. Pichot, L. Chahed, Y. Cuminal. Amorphous-nanocrystalline transition in silicon thin films obtained by argon diluted silane PECVD. *Cryst. Struct. Theory Appl.* **1**, 57 (2012).
12. G. Fugallo, A. Mattoni. Thermally induced recrystallization of textured hydrogenated nanocrystalline silicon. *Phys. Rev. B* **89**, 045301 (2014).
13. O. Nast, A.J. Hartmann. Influence of interface and Al structure on layer exchange during aluminum-induced

crystallization of amorphous silicon. *J. Appl. Phys.* **88**, 716 (2000).
14. M. Jeon, C. Jeong, K. Kamisako. Tin induced crystallisation of hydrogenated amorphous silicon thin films. *Mater. Sci. Technol.* **26**, 875 (2010).
15. M.A. Mohiddon, M.G. Krishna. Growth and optical properties of Sn–Si nanocomposite thin films. *J. Mater. Sci.* **47**, 6972 (2012).
16. D. Van Gestel, I. Gordon, J. Poortmans. Aluminum-induced crystallization for thin-film polycrystalline silicon solar cells: Achievements and perspective. *Sol. Energy Mater. Sol. Cells* **119**, 261 (2013).
17. A. Mohiddon, G. Krishna. Metal induced crystallization. in *Crystallization – Science and Technology*, edited by A. Marcello (InTech, 2012), p. 461 [ISBN: 978-953-51-0757-6].
18. V.V. Voitovych, V.B. Neimash, N.N. Krasko, A.G. Kolosiuk, V.Y. Povarchuk, R.M. Rudenko, V.A. Makara, R.V. Petrunya, V.O. Juhimchuk, V.V. Strelchuk. The effect of Sn impurity on the optical and structural properties of thin silicon films. *Semiconductors* **45**, 1281 (2011).
19. V.B. Neimash, V.M. Poroshin, A.M. Kabaldin, V.O. Yukhymchuk, P.E. Shepelyavyi, V.A. Makara, S.Y. Larkin. Paper abstract microstructure of thin Si–Sn composite films. *Ukr. J. Phys.* **58**, 865 (2013).
20. V. Neimash, V. Poroshin, P. Shepeliavyi, V. Yukhymchuk, V. Melnyk, A. Kuzmich, V. Makara, A.O. Goushcha. Tin induced a-Si crystallization in thin films of Si–Sn alloys. *J. Appl. Phys.* **114**, 213104 (2013).
21. V.B. Neimash, A.O. Goushcha, P.E. Shepeliavyi, V.O. Yukhymchuk, V.A. Dan'ko, V.V. Melnyk, A.G. Kuzmich. Mechanism of tin-induced crystallization in amorphous silicon. *Ukr. J. Phys.* **59**, 1168 (2014).
22. V.B. Neimash, A.O. Goushcha, P.Y. Shepeliavyi, V.O. Yukhymchuk, V.A. Danko, V.V. Melnyk, A.G. Kuzmich. Self-sustained cyclic tin induced crystallization of amorphous silicon. *J. Mat. Res.* **30**, 3116 (2015).
23. V. Neimash, P. Shepelyavyi, G. Dovbeshko, A.O. Goushcha, M. Isaiev, V. Melnyk, O. Didukh, A. Kuzmich. Nanocrystals growth control during laser annealing of Sn:(α-Si) composites. *J. Nanomater.* **2016**, 1 (2016).
24. H. Richter, Z.P. Wang, L. Ley. The one phonon Raman spectrum in microcrystalline silicon. *Solid State Commun.* **39**, 625 (1981).
25. I.H. Campbell, P.M. Fauchet. The effects of microcrystal size and shape on the one phonon Raman spectra of crystalline semiconductors. *Solid State Commun.* **58**, 739 (1986).
26. A. Hiraki. Low temperature reactions at Si/metal interfaces: What is going on at the interfaces? *Surf. Sci. Reports* **3** (7), 357 (1983).
27. S.A. Akhmanov, V.I. Emel'yanov, N.I. Koroteev, V.N. Seminogov. Interaction of powerful laser radiation with the surfaces of semiconductors and metals: Nonlinear optical effects and nonlinear optical diagnostics. *Usp. Fiz. Nauk* **147**, 675 (1985) (in Russian).
28. R. Burbelo, D. Andrusenko, M. Isaiev, A. Kuzmich. Laser photoacoustic diagnostics of advanced materials with different structure and dimensions. *Arch. Metall. Mater.* **56**, 1157 (2011).
29. R. Burbelo, M. Isaiev, A. Kuzmich. Evolution of temperature distribution in implanted Si-based structures: Pulse mode of laser irradiation. *Ukr. J. Phys.* **55**, 317 (2010).
30. M. Isaiev, V. Kuryliuk, A. Kuzmich, R. Burbelo. Photothermal transformation in heterogeneous semiconductors structures under its pulse laser irradiation: Role of electron-hole diffusion. *Arch. Metall. Mater.* **58**, 15 (2013).
31. G. Grimvall. *Thermophysical Properties of Materials* (The Royal Institute of Technology, 1999) [ISBN: 9780080542867].
32. G.K.M. Thutupalli, S.G. Tomlin. The optical properties of amorphous and crystalline silicon. *J. Phys. C* **10**, 467 (1977).
33. S. Adachi, H. Mori. Optical properties of fully amorphous silicon. *Phys. Rev. B* **62**, 10158 (2000).
34. D.R. Queen. *The Specific Heat of Pure and Hydrogenated Amorphous Silicon* (Univ. of California, 2011).
35. B.L. Zink, R. Pietri, F. Hellman. Thermal conductivity and specific heat of thin-film amorphous silicon. *Phys. Rev. Lett.* **96**, 55902 (2006).
36. S.P. Rodichkina, L.A. Osminkina, M. Isaiev, A.V. Pavlikov, A.V. Zoteev, V.A. Georgobiani, K.A Gonchar, A.N. Vasiliev, V.Y. Timoshenko. Raman diagnostics of photoinduced heating of silicon nanowires prepared by metal-assisted chemical etching. *Appl. Phys. B* **121**, 337 (2015).
37. M. Isaiev, O. Didukh, T. Nychyporuk, V. Timoshenko, V. Lysenko. Anisotropic heat conduction in silicon nanowire network revealed by Raman scattering. *Appl. Phys. Lett.* **110**, 011908 (2017).
38. O. Plaksin, Y. Takeda, H. Amekura, N. Kishimoto, S. Plaksin. Saturation of nonlinear optical absorption of metal-nanoparticle composites. *J. Appl. Phys.* **103**, 114302 (2008).
39. G. Conibeer. Third-generation photovoltaics. *Mater. Today* **10**, 42 (2007).
40. G. Conibeer, I. Perez-Wurfl, X. Hao, D. Di, D. Lin. Si solid-state quantum dot-based materials for tandem solar cells. *Nanoscale Res. Lett.* **7**, 193 (2012).
41. V.G. Litovchenko. On some important results in semiconductor surface science obtained in Ukraine during the independence years (1991—2016). *Ukr. J. Phys.* **62**, 80 (2017).
42. V.G. Litovchenko, T.I. Gorbanyuk, V.S. Solntsev, A.A. Evtukh. Mechanism of hydrogen, oxygen and humidity sensing by Cu/Pd-porous silicon-silicon structures. *Appl. Surf. Sci.* **234**, 262 (2004).
43. V.G. Litovchenko, T.I. Gorbanyuk, V.S. Solntsev, A.A. Evtukh. Mechanism of hydrogen-containing and oxygen molecules sensing by Pd- and Cu/Pd-porous Si-Si structures. *Appl. Surf. Sci.* **234**, 262 (2004).
44. V. Lysenko, J. Vitiello, B. Remaki, D. Barbier, V. Skryshevsky. Nanoscale morphology dependent hydrogen coverage of meso-porous silicon. *Appl. Surf. Sci.* **230**, 425 (2004).

Received 19.07.17.
Translated from Ukrainian by O.I. Voitenko

В.Б. Неймаш, В. Мельник,
Л.Л. Федоренко, П.Є. Шепелявий, В.В. Стрільчук,
А.С. Ніколенко, М.В. Ісаєв, А.Г. Кузьмич

ІНДУКОВАНА ОЛОВОМ КРИСТАЛІЗАЦІЯ АМОРФНОГО КРЕМНІЮ ПРИ ІМПУЛЬСНОМУ ЛАЗЕРНОМУ ОПРОМІНЕННІ

Р е з ю м е

Методом комбінаційного розсіювання світла досліджено процеси індукованої оловом кристалізації аморфного кремнію в тонкоплівкових структурах Si–Sn–Si під дією різних видів імпульсного лазерного опромінення. Експериментально визначено та проаналізовано залежності розмірів та концентрації нанокристалів Si від потужності лазерних імпульсів тривалістю 10 нс та 150 мкс з довжиною хвилі 535 нм та 1070 нм. Показано можливість ефективної індукованої оловом трансформації кремнію із аморфної фази в кристалічну за час порядку 10 нс в шарах a–Si товщиною 200 нм під дією імпульсу лазерного світла. Теоретичний розрахунок просторового і часового розподілу температур в зоні дії лазерного променя використано для інтерпретації експериментальних результатів.